Variation between Antiferromagnetism and Ferrimagnetism in NiPS₃ by Electron Doping

Mengjuan Mi[1][#], Xingwen Zheng[2][#], Shilei Wang[3][#], Yang Zhou[2], Lixuan Yu[1], Han Xiao[1], Houning Song[2], Bing Shen[4], Fangsen Li[5], Lihui Bai[2], Yanxue Chen[2*], Shanpeng Wang[3*], Xiaohui Liu[2*], Yilin Wang[1*]

[1]School of Microelectronics, Shandong Technology Center of Nanodevices and Integration, State Key Laboratory of Crystal Materials, Shandong University, Jinan 250100, China.

[2]School of Physics, Shandong University, Jinan 250100, China.

[3]State Key Laboratory of Crystal Materials, Institute of Crystal Materials, Shandong University, Jinan, 250100, China.

[4]School of Physics, Sun Yat-Sen University, Guangzhou 510275, China.

[5]Vacuum Interconnected Nanotech Workstation, Suzhou Institute of Nano-Tech and Nano-Bionics, Chinese Academy of Sciences, Suzhou 215123, China.

[#]These authors contributed equally.

*Correspondence and requests for materials should be addressed to: Y.W. (email: yilinwang@email.sdu.edu.cn); X.L. (liuxiaohui@sdu.edu.cn); S.W. (wshp@sdu.edu.cn); Y.C. (cyx@sdu.edu.cn)

Abstract:

How to electrically control magnetic properties of a magnetic material is promising towards spintronic applications, where the investigation of carrier doping effects on antiferromagnetic (AFM) materials remains challenging due to their zero net magnetization. In this work, we found electron doping dependent variation of magnetic orders of a two-dimensional (2D) AFM insulator $NiPS_3$, where doping concentration is tuned by intercalating various organic cations into the van der Waals gaps of $NiPS_3$ without introduction of defects and impurity phases. The doped $NiPS_3$ shows an AFM-ferrimagnetic (FIM) transition at doping level of 0.2-0.5 electrons/cell and a FIM-AFM transition at doping level of ≥ 0.6 electrons/cell. We propose that the found phenomenon is due to competition between Stoner exchange dominated inter-chain ferromagnetic order and super-exchange dominated inter-chain AFM order at different doping level. Our studies provide a viable way to exploit correlation between electronic structures and magnetic properties of 2D magnetic materials for realization of magnetoelectric effect.

1. Introduction

Since the first experimental observation of intrinsic ferromagnetism in monolayer CrI$_3$[1] and bilayer Cr$_2$Ge$_2$Te$_6$[2], van der Waals (vdW) magnetic materials have attracted extensive attention in both fundamental research and practical applications[3-9]. The field of two-dimensional (2D) magnetic materials grows rapidly and various types of 2D magnetic materials have been discovered and synthesized, such as ferromagnetic (FM) magnets including Cr$_2$Ge$_2$Te$_6$[2], CrBr$_3$[10], Fe$_3$GeTe$_2$[11,12], Fe$_5$GeTe$_2$[13], monolayer VSe$_2$[14], etc., and antiferromagnetic (AFM) magnets including CrCl$_3$[15], transition metal phosphorous trichalcogenides MPX$_3$ (M = Mn, Fe, Ni; X = S, Se)[16-19], CrPS$_4$[20], MnBi$_2$Te$_4$[21], etc. The distinct spin-dependent properties of these materials provide a promising platform for the discovery and study of new quantum phenomena and design of novel spintronic devices.

Due to the ultrathin thickness and weak interlayer vdW interaction of 2D magnetic materials, their magnetic properties, such as Curie temperature, magnetic anisotropy, saturation magnetization, and coercive force can be effectively modulated by magnetic field[1], electric field[22], strain[23], electrostatic doping[11,24-27], and ion intercalation[28], etc. Several studies have demonstrated the carrier doping dependent changes in magnetic properties of CrI$_3$[24], Cr$_2$Ge$_2$Te$_6$[26,28], and Fe$_3$GeTe$_2$[11], which are attributed to carrier doping induced change on exchange interaction due to orbital occupation of transition metal atoms in these materials. The modulation of magnetic properties by carrier doping serves as a viable tool for realizing effective magnetoelectric coupling and is promising for designing electric-field controlled spintronic devices. However, among these impressive studies, experimental realization of carrier doping induced AFM-FM transition in 2D magnetic materials has rarely been reported[24] and the mechanism responsible for the magnetic transition is not clear and needs to be further explored.

Among various magnetic materials, MPX$_3$ compounds are of great interest for their rich variety of electronic and magnetic properties depending on the role of the transition metal elements[16-19,29,30]: Heisenberg-type MnPS$_3$, Ising-type FePS$_3$, and XY

65 or XXZ-type NiPS$_3$. MPX$_3$ compounds have been theoretically predicted to exhibit

66 strong charge-spin coupling[31,32] and carrier doping dependent AFM-FM transition[33,34],

67 while experimental studies are lack.

68   In this work, we report on the electron doping dependent AFM-FIM transition in

69 a self-doped AFM insulator NiPS$_3$, where the electron doping is realized by

70 intercalating organic cations into the van der Waals gaps[35]. Intercalation has been

71 demonstrated to be an effective method to dope electrons into 2D materials and

72 modulate their electronic, optical, magnetic, and superconducting properties[28,36-40].

73 We found variation of magnetic order from AFM to FIM and then AFM with the

74 increasing of electron concentration. Our experimental results are consistent with

75 theoretical analysis based on the first-principles calculations. We propose that such

76 AFM-FIM transition at low electron doping level originates from the Stoner exchange

77 due to the self-doped feature of NiPS$_3$ which provides effective inter-chain itinerant

78 channel. The FIM-AFM transition at high electron doping level is due to the rise of

79 inter-chain super-exchange. Our studies provide a new insight into the carrier doping

80 tuned magnetic transition in 2D magnetic materials.

81 ## 2. Results and Discussion

82   Figure 1(a) shows the crystal and magnetic structures of NiPS$_3$[29,30,41,42]. Bulk

83 NiPS$_3$ has a monoclinic structure (*C2/m*), where two P atoms (P-P pair) are covalently

84 bonded to six S atoms to form a $(P_2S_6)^{4-}$ anion complex, and each Ni atom carries a

85 +2 electronic ionization state and lies on a honeycomb lattice in the *ab* plane. The

86 layers in the *ab* plane are coupled by weak vdW interactions along the *c*-axis, and the

87 interlayer distance is 6.34 Å. Below Néel temperature (T_N~150 K), magnetic moments

88 are aligned mostly in the *ab* plane (along the a-axis direction) with a small

89 out-of-plane component, and each Ni^{2+} ion is coupled ferromagnetically to two of the

90 nearest neighbors and antiferromagnetically to the third one, forming zigzag

91 ferromagnetic chains (parallel to the a-axis) coupled antiferromagnetically to each

92 other along the b-axis direction (zigzag AFM order, upper panel in Figure 1(a)). The

93 non-equivalent Ni^{2+} ions in two adjacent ferromagnetic zigzag chains are marked as

94   Ni(1) and Ni(2), respectively.

95   Intercalation offers a versatile approach for tuning charge carriers in 2D

96   materials due to the charge transfer between guest intercalants and host 2D materials[35].

97   Because of the remarkable wide vdW gap in MPX$_3$, guest intercalants can be easily

98   intercalated into the vdW gaps, and these compounds have been extensively studied

99   as cathodic materials in lithium batteries[43]. High-quality NiPS$_3$ bulk crystals were

100   used as the host materials, and electrochemical intercalation method was adopted to

101   insert organic cations, such as THA$^+$, into the vdW gaps of NiPS$_3$, as shown in Figure

102   1(a). The successful intercalation is confirmed by X-ray diffraction (XRD)

103   measurement as shown in Figure 1(b), where the obvious shift of diffraction peaks to

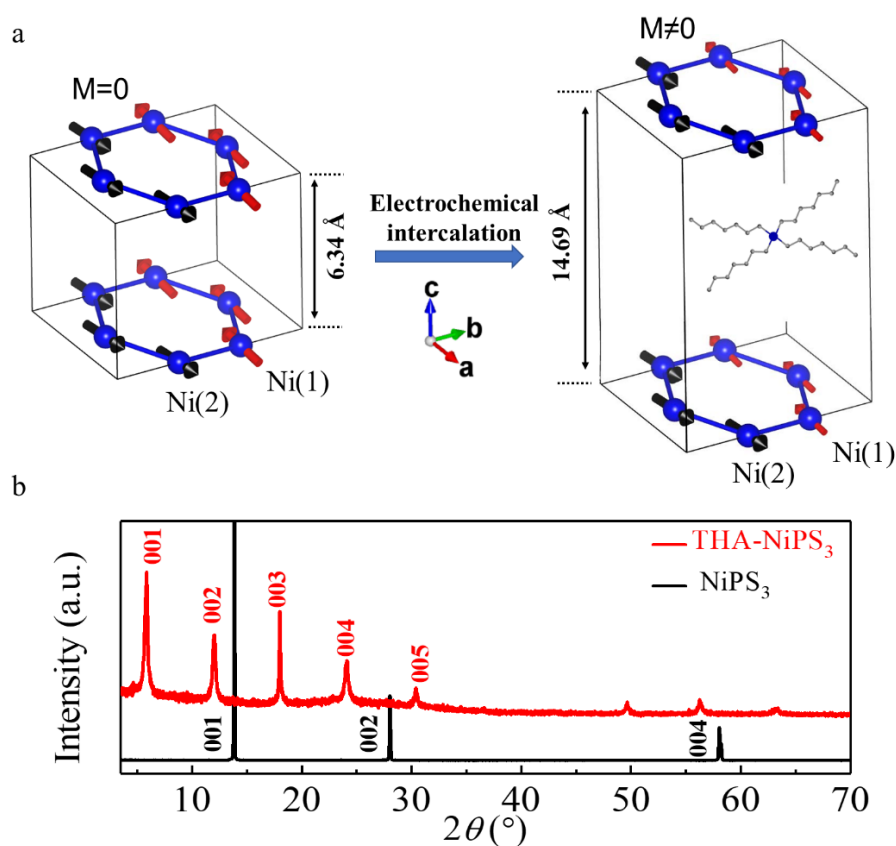104   smaller angles indicates that the interlayer distance is expanded to 14.69 Å.

105

106   **Fig. 1** Structures of pristine NiPS$_3$ and intercalated THA-NiPS$_3$. **a** Structures of NiPS$_3$
107   (left) and THA$^+$ cations intercalated NiPS$_3$ (THA-NiPS$_3$, right). Arrows indicate the
108   orientation and size of magnetic moments of Ni atoms, and the Ni atoms in two
109   adjacent zigzag ferromagnetic chains are marked as Ni(1) and Ni(2), respectively. **b**
110   XRD patterns of pristine NiPS$_3$ and intercalated THA-NiPS$_3$.

111   Figure 2 shows the temperature-dependent magnetization (M-T) and

112   field-dependent magnetization (M-H) for pristine $NiPS_3$ and intercalated THA-$NiPS_3$

113   with a magnetic field applied along directions parallel to the *ab* plane and

114   perpendicular to the *ab* plane (*c**). The overall behavior of pristine $NiPS_3$ is consistent

115   with previous results, and a typical AFM characteristic is observed[29,30]. No substantial

116   difference is observed between the field-cooled (FC) and zero-field cooled (ZFC)

117   measurements. The broad maximum at elevated temperatures is related to the

118   short-range spin correlations. The Néel temperature, T_N, defined from the sharp peak

119   in the derivative dM/dT for H // *ab* is ~150 K (inset of Figure 2(a)). Below T_N, with

120   respect to the magnetization for H // *c**, the magnetization for H // *ab* decreases

121   rapidly and reaches a smaller value at low temperature (Figure 2(a)), indicating that

122   the magnetic moments lie mostly in the *ab* plane. A linear dependence of M *vs* H for

123   H // *c** is observed, while a clear upturn in M *vs* H for H // *ab* above a critical field

124    $\mu_0 H$~5T is observed (Figure 2(b)). The upturn in the magnetization at high field may

125   be attributed to the spin-flop transition in pristine $NiPS_3$[44].

126   After intercalation, an obvious FIM characteristic (discuss in detail later) with a

127   Curie temperature T_c~100 K is observed in THA-$NiPS_3$. As shown in Figures

128   2(c)-2(d), for H // *ab*, the magnetization increases rapidly below 100 K, and an

129   obvious magnetic hysteresis loop is observed at a low temperature, which provides an

130   unambiguous identification of FIM order. For H // *c**, the magnetization is

131   significantly smaller, and a linear dependence of M *vs* H is observed, which suggests

132   that the large magnetic anisotropy still remains in intercalated THA-$NiPS_3$, and the

133   FIM easy axis still lies in the *ab* plane. With increasing temperature (Figures

134   2(e)-2(f)), the magnetic hysteresis loop becomes less obvious, and both remnant

135   magnetization and coercive field become smaller monotonically. The M-H curve

136   shows a linear dependence at T = 100 K (inset in Figure 2(e)), indicating a

137   FIM-paramagnetic transition, which is consistent with the M-T curves in Figure 2(c).
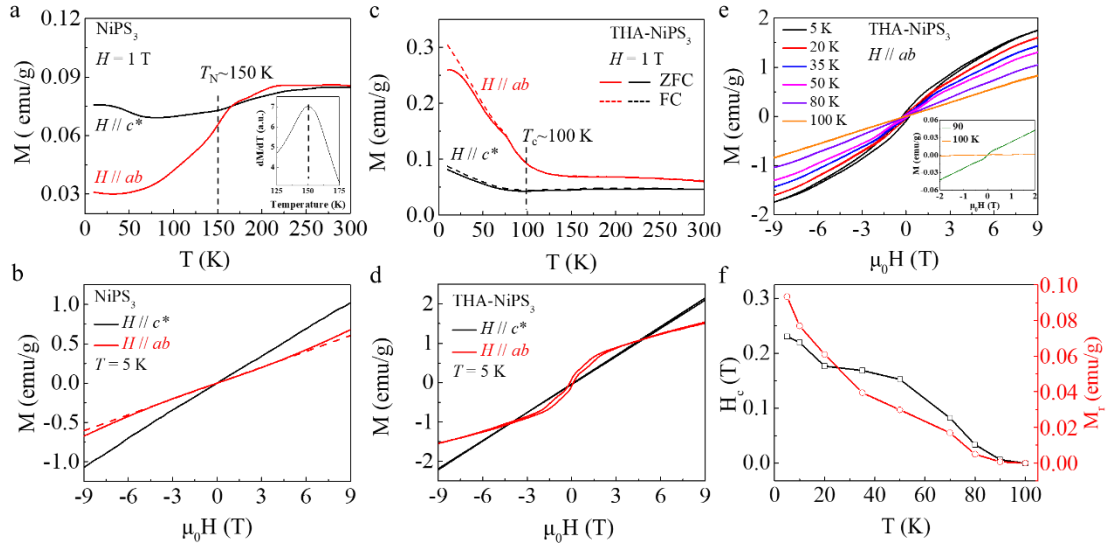
Fig. 2 Magnetic properties of pristine NiPS$_3$ and intercalated THA-NiPS$_3$. **a, b** Temperature dependence of magnetization (*M-T*, **a**) in zero-field cooled (ZFC) mode and field dependence of magnetization (*M-H*, **b**) of pristine NiPS$_3$ under magnetic fields *H // ab* (red) and *H // c** (black). **c, d** Temperature dependence of magnetization (*M-T*, **c**) and field dependence of magnetization (*M-H*, **d**) of intercalated THA-NiPS$_3$ under magnetic fields *H // ab* (red) and *H // c** (black). The solid and dashed lines in **c** represent zero-field cooled (ZFC) and field cooled (FC) data, respectively. **e** Isothermal magnetization of intercalated THA-NiPS$_3$ under a magnetic field *H // ab* at different temperatures. Inset shows enlarged *M-H* data at 90 K and 100 K after subtracting a linear fitting. **f** Extracted remnant magnetization M_r (red) and coercive field H_c (black) of intercalated THA-NiPS$_3$ as a function of temperature.

What causes the magnetic transition from AFM in pristine NiPS$_3$ to FIM in intercalated THA-NiPS$_3$? Whether such AFM- FIM transition originates from defects or impurity phases? To solve these puzzles, detailed structural and chemical characterizations were carried out. Figure 3 shows typical morphologies of exfoliated pristine NiPS$_3$ and intercalated THA-NiPS$_3$ thin flakes. The intercalated THA-NiPS$_3$ has a flat and smooth surface, and no obvious defects are observed. After intercalation, the root-mean-square (RMS) roughness slightly increases from 0.2 nm (pristine NiPS$_3$) to 0.35 nm (THA-NiPS$_3$). A step height of ~1.6 nm is observed for THA-NiPS$_3$ (see supplementary Fig. S1), which is consistent with the XRD results. We provided the first experimental evidence showing that the organic cations intercalated 2D materials host a platform for the atomic-scale investigation by scanning probe techniques.
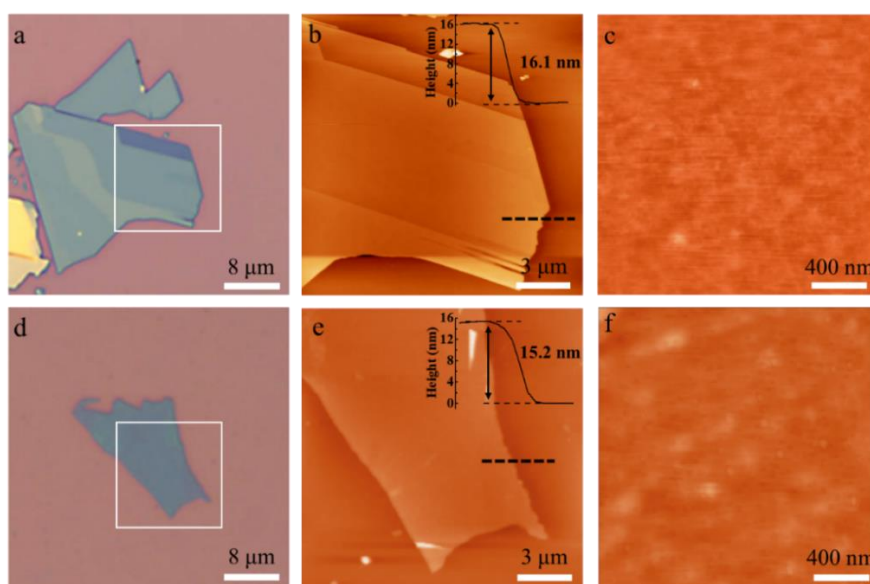
Fig. 3 Surface morphologies of pristine NiPS$_3$ and intercalated THA-NiPS$_3$. **a-c** Optical image (**a**), AFM image (**b**) and zoomed-in AFM image (**c**) of exfoliated pristine NiPS$_3$. **d-f** Optical image (**d**), AFM image (**e**) and zoomed-in AFM image (**f**) of exfoliated intercalated THA-NiPS$_3$. Insets in **b** and **e** indicate the thickness line profiles of pristine NiPS$_3$ and intercalated THA-NiPS$_3$, respectively.

We investigate whether defects are formed in intercalated THA-NiPS$_3$ by Raman spectroscopy, which is an eminent technique for the characterization of many properties, such as the number of layers, strain, disorder, and defect density, etc., of 2D materials[45]. Figure 4(a) compares the Raman spectra of bulk pristine NiPS$_3$ and bulk intercalated THA-NiPS$_3$. Eight Raman-active phonon modes (three out-of-plane A$_{1g}$ modes and five in-plane E$_g$ modes) are observed in pristine NiPS$_3$, which is consistent with previous results[16]. For intercalated THA-NiPS$_3$, most peaks of pristine NiPS$_3$ are still observed, and a new peak near 206 cm^{-1} that is absent in bulk pristine NiPS$_3$ appears. This peak is ascribed to the resonance-enhanced multi-phonon scattering, and is only observed in ultrathin NiPS$_3$ flakes[16,42]. The evolution of three out-of-plane modes (A_{1g}^1, A_{1g}^2, and A_{1g}^3, which are sensitive to interlayer coupling) of NiPS$_3$ after intercalation is consistent with the results of pristine NiPS$_3$ as thickness decreases (see supplementary Fig. S2)[42]. The Raman spectroscopy of intercalated THA-NiPS$_3$ is very similar to that of exfoliated monolayer NiPS$_3$[16], and no signature related to defects and strain was observed, indicating that the intercalated organic cations effectively reduce interactions between adjacent layers without breaking the

183   in-plane covalent bonds.

184   We further investigate whether impurity phases are formed in intercalated
185   THA-NiPS$_3$ by X-ray photoelectron spectroscopy (XPS), which identifies the
186   chemical shift caused by electron state surrounding the atoms of NiPS$_3$ after
187   intercalation, and the results are shown in Figure 4(b). For pristine NiPS$_3$, the Ni 2p
188   spectrum consists of two main peaks located at binding energies of 854.5 eV and
189   871.8 eV accompanied with satellite peaks, which correspond to 2p$_{3/2}$ and 2p$_{1/2}$ levels,
190   respectively. After intercalation, both Ni 2p$_{3/2}$ and Ni 2p$_{1/2}$ peaks obviously shift
191   towards lower binding energies and the intensities of the satellite peaks are weakened,
192   which is consistent with the results in lithium intercalated NiPS$_3$ (Li$_x$NiPS$_3$)[46].
193   Similarly, both P 2p spectrum (2p$_{3/2}$ and 2p$_{1/2}$) and S 2p spectrum (2p$_{3/2}$ and 2p$_{1/2}$) shift
194   towards lower binding energies after intercalation (see supplementary Table 1). No
195   signature indicative of impurity phases was observed, and the shift of XPS peaks
196   towards lower binding energies clearly indicates that the intercalation of THA$^+$
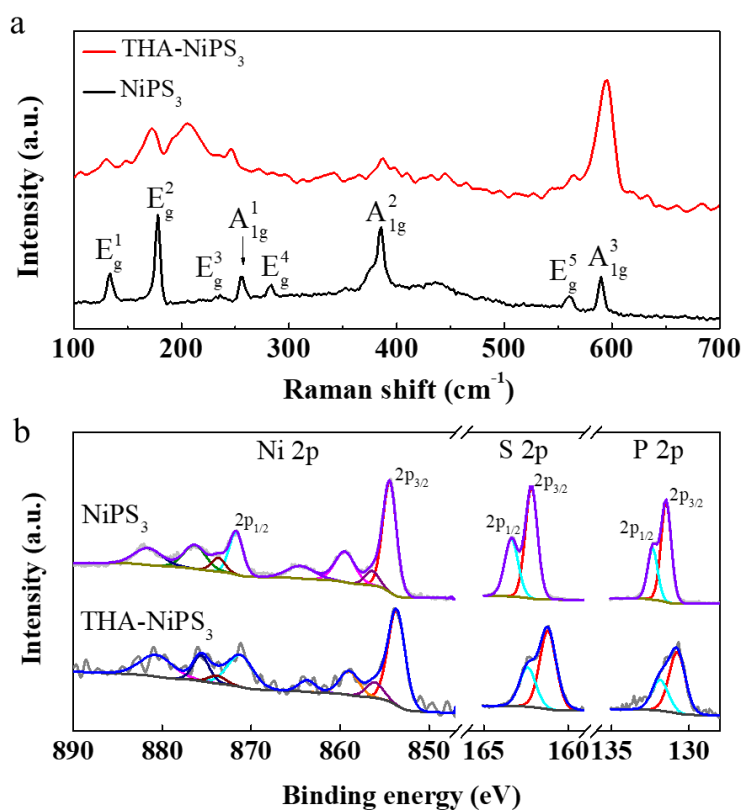197   cations leads to electron doping[35].

198
199   **Fig. 4** Raman (**a**) and XPS (**b**) spectra of pristine NiPS$_3$ and intercalated THA-NiPS$_3$.

200   The intercalated THA$^+$ cations decouple the interactions between adjacent NiPS$_3$

201   layers and lead to electron doping of NiPS$_3$ without introducing obvious strain,

202   defects, and impurities phases. To understand the effects of electron doping on the

203   electronic and magnetic properties of NiPS$_3$, we performed first-principles

204   calculations with Quantum-ESPRESSO[47]. Figure 5(a) shows the calculated band

205   structure of pristine NiPS$_3$, where we could see an isolated narrow conduction band

206   which is dominated by the Ni-d orbitals (d$_{zx}$, d$_{zy}$, and d$_{xy}$) and contributed by S-p

207   orbitals. Without doping, the electronic bands are spin degenerate. Inner-chain

208   magnetic order is ferromagnetic carrying a magnetic moment of 1.51 μ_B per Ni atom,

209   and the inter-chain magnetic order is antiferromagnetic as shown in Figure 1(a),

210   which agrees well with previous studies.

211   Figure 5(b) shows atom projected density of states (PDOS) of NiPS$_3$ with

212   different doping concentrations, which illustrates the evolution of the electronic

213   structure as a function of doping levels. With light doping concentration of 0.1

214   electrons/cell, no change occurs on the band. With moderate doping concentrations of

215   0.2-0.5 electrons/cell, we could see obvious splitting on both orbitals and spin states,

216   and the splitting gets larger with doping concentration increased. With further

217   increasing doping concentration to above 0.6 electrons/cell, the spin-polarization

218   disappears and the system goes back to zigzag AFM order, while the splitting of

219   orbitals still exists. The vanishing of spin-polarization is due to the rise of

220   super-exchange between the two zigzag chains through the S-p states.

221   To understand the variation of magnetic structures with doping concentrations,

222   we further calculated the orbital-resolved band structure (right panel in Figure 5(a))

223   and projected density of states (PDOS) of Ni atom on each ferromagnetic chain with

224   opposite orientation of magnetic moments (Ni(1) site and Ni(2) site) at different

225   doping concentrations (as shown in Figure 5(c)). Interestingly, we could see that the

226   splitting causes the doped electrons to occupy Ni atoms at one zigzag ferromagnetic

227   chain with moderate doping concentration of 0.2-0.5 electrons/cell, and a net

228   magnetic moment shows up (discuss in details later). This phenomenon may be

229   understood from Stoner model, which is based on the competition between kinetic

230   energy and exchange energy and is common in material with narrow conduction band.

231   From the calculations, we could see that the conduction band minimum (CBM) is

232   dominated by d_{zx}, d_{zy}, and d_{xy} orbitals of Ni atoms. As doping concentration increases,

233   due to the electron correlation, the d_{zy} orbital is further pushed up and the CBM is

234   then dominated by d_{zx} and d_{xy} orbitals, which are mainly overlapped in the inter-chain

235   direction, and the overlapping is responsible for the doped electrons to be inter-chain

236   itinerant and lead to Stoner effect induced inter-chain spin splitting.

237   In fact, $NiPS_3$ is a self-doped insulator[31], the S atoms that separate the Ni chains

238   are not fully occupied. Therefore, after doping electrons, the not fully occupied S-p

239   orbital provides a channel for the electrons to be itinerant between the Ni chains.

240   Further, the feature of narrow bands of d orbital makes the density of states large,

241   which is necessary for the Stoner splitting of the itinerant electrons between the Ni

242   chains. With light doping, even though the electrons is inter-chain itinerant, the small

243   DOS close to the CBM is not able to trigger the Stoner effect. However, we could see

244   that the DOS is sharp near the CBM. With doping concentration increases, the DOS

245   on Fermi level increases quickly. When the doping concentration increases to 0.2

246   electrons/cell, the DOS at Fermi level is large enough to result in Stoner splitting.

247   Thus, the doped electrons only occupy one Ni chain, which results in the net magnetic

248   moment we found in experiment. However, when the doping concentration further

249   increases to over 0.6 electrons/cell, the super-exchange between the chains through

250   the S 2p orbital starts to dominate the magnetic order. Because the d orbital of Ni is

251   more than half occupied, the super-exchange effect leads to antiferromagnetic order

252   between chains and the net magnetic moment disappears. Figure 5(d) shows the

253   magnetic moments on Ni(1) and Ni(2) with different doping concentrations, and the

254   right panel in Figure 1(a) shows a schematic of the magnetic moments on Ni(1) and

255   Ni(2) at moderate doping level, which give a more direct picture of the evolution of

256   the magnetic order of the two chains. At an appropriate doping concentration, the

257   antiferromagnetically coupled two zigzag ferromagnetic chains carry unequal

258   magnetic moments, which leads to the net magnetic moments and FIM characteristics
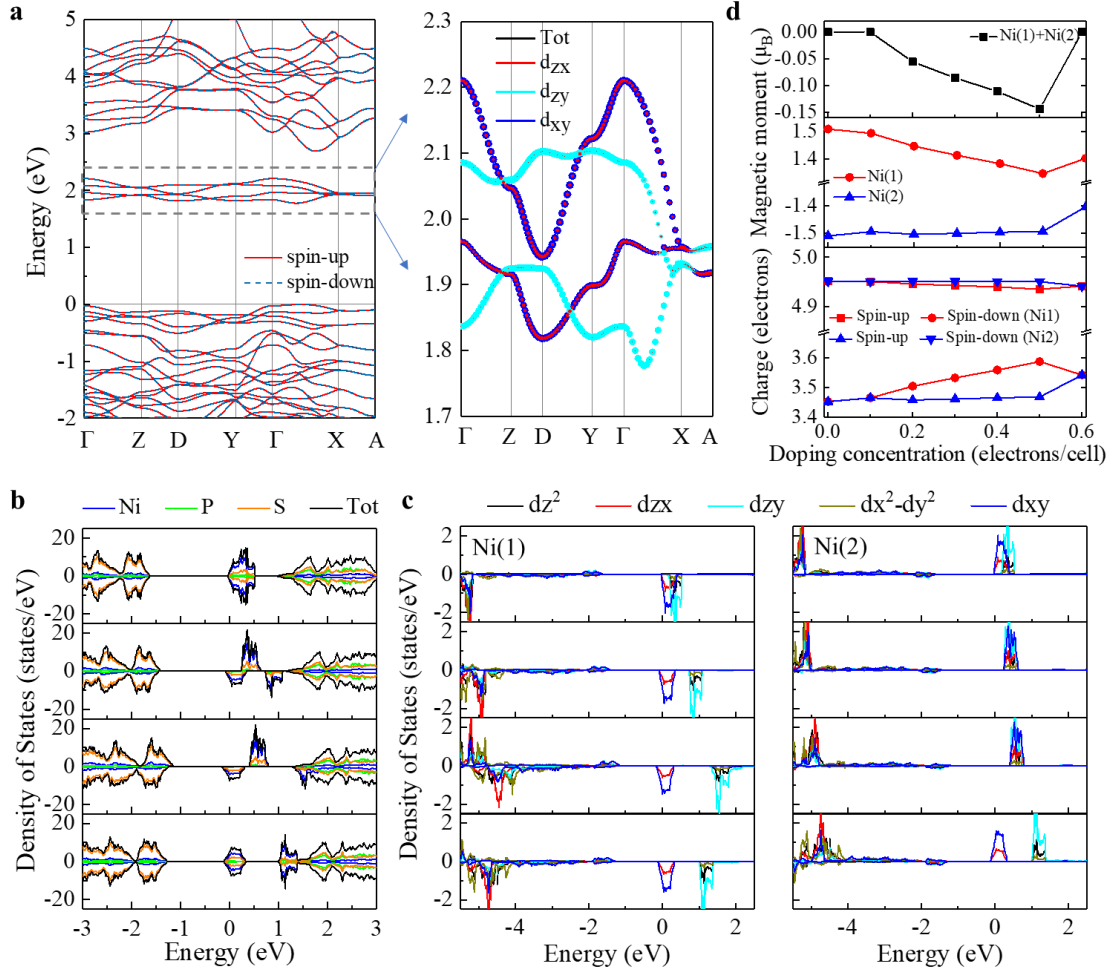
259   in intercalated THA-$NiPS_3$.

Fig. 5 Band structures and electronic properties of NiPS$_3$ at different doping concentrations. **a** Band structure of spin-up and spin-down configurations of pristine NiPS$_3$ (left) and enlarged region of conduction band minimum (right), the orbital characters of bands are represented by different colors. **b** Element-resolved projected density of states (PDOS) of NiPS$_3$ with doping concentrations of 0.1, 0.2, 0.5 and 0.6 electrons/cell from top to bottom. **c** Ni's d-orbital resolved PDOS with doping concentrations of 0.1, 0.2, 0.5 and 0.6 electrons/cell from top to bottom of Ni (1) (left) and Ni (2) (right). **d** Net magnetic moments (top), magnetic moments of Ni (1) and Ni (2) (middle) and charges of Ni (1) and Ni (2) with spin-up and spin-down configurations (bottom) as a function of doping concentrations. A doping concentration of 0.1 electrons/cell corresponds to an electron density of 0.8×10^{13} cm^{-2}.

We further quantitatively compare the experimental results with the calculated theoretical values. The observed FIM signal of THA-NiPS$_3$ is weak, and the corresponding average net magnetic moment per cell is approximately 0.07 μ_B, which lies in the range of theoretically expected values. Due to the highly insulating property of NiPS$_3$ (conductivity ~10^{-7} S/cm at room temperature[42]) and degradation of

278   intercalated $NiPS_3$ during device fabrication process, quantitative determining the

279   carrier density in intercalated $NiPS_3$ is challenging. Previous studies have shown that

280   intercalated THA^+ cations cause a doping concentration of 0.02 electrons per MoS_2

281   formula unit[37] (corresponding to a carrier density of 2.3×10^{13} cm^{-2}), assuming that

282   intercalated THA^+ cations cause a similar doping concentration in $NiPS_3$, which lies

283   in the appropriate doping concentration that leads to the net magnetic moment.

284   The induced doping concentration is strongly dependent on the species of

285   intercalated organic cations, for example, cations such as tetrabutyl ammonium

286   (TBA^+), tetrapropyl ammonium (TPA^+), and cetyltrimethyl ammonium (CTA^+) cause

287   a substantially large doping concentration ($>10^{14}$ cm^{-2}) in intercalated 2D

288   materials[28,37,38]. The conductivity of $NiPS_3$ increases with increasing doping

289   concentration in lithium intercalated $NiPS_3$[48]. We measured conductivities of $NiPS_3$

290   intercalated with various organic cations (see supplementary Fig. S6). After

291   intercalation, the conductivity of $NiPS_3$ increases, and the conductivities of

292   TBA-$NiPS_3$, TPA-$NiPS_3$ and CTA-$NiPS_3$ are significantly greater than that of

293   THA-$NiPS_3$, confirming that intercalated TBA^+, TPA^+, and CTA^+ cations cause a

294   greater doping concentration than intercalated THA^+ cations. Similar to THA-$NiPS_3$,

295   the interlayer distance increases to 11.46 Å, 12.14 Å and 14.82 Å for TBA-$NiPS_3$,

296   TPA-$NiPS_3$ and CTA-$NiPS_3$ (as shown in Figure 6(a)), respectively, and the Raman

297   spectra of TBA-$NiPS_3$, TPA-$NiPS_3$ and CTA-$NiPS_3$ also exhibit characteristics of

298   monolayer $NiPS_3$ sheet (see supplementary Fig. S6(a)). As predicted by our

299   theoretical model that the net magnetic moment disappears at high doping

300   concentration, we do not observe any FIM characteristics in the heavily doped $NiPS_3$

301   samples, except a linear dependence of *M vs H* (as shown in Figure 6(b)). These

302   results rule out the possibility of causing magnetic transition in $NiPS_3$ by strain,

303   defects and impurity phases, and further confirm the role of carrier doping in tuning
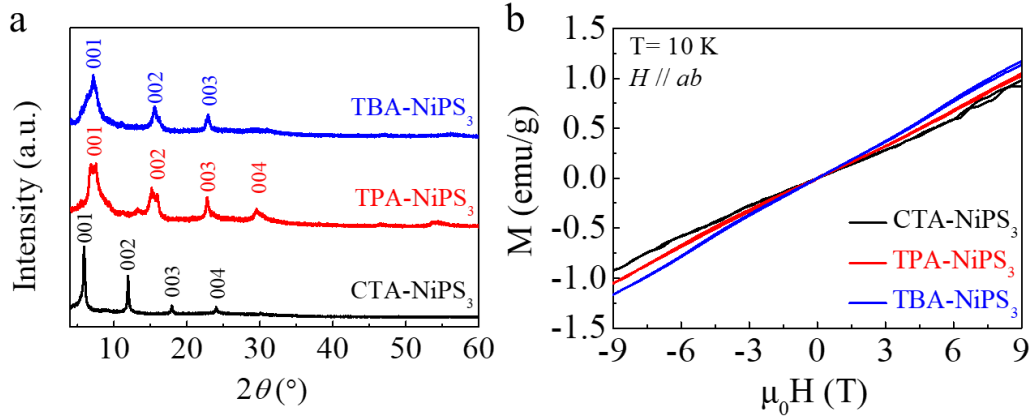
304   the magnetic properties of $NiPS_3$.

Fig. 6 XRD patterns (**a**) and field dependence of magnetization (*M-H*, **b**) measured under magnetic field *H // ab* at 10 K of intercalated TBA-NiPS$_3$, TPA-NiPS$_3$, and CTA-NiPS$_3$.

3. Conclusions

We successfully realized the AFM-FIM-AFM transition in NiPS$_3$ with carrier doping by intercalating organic cations into vdW gaps of NiPS$_3$. The intercalated organic cations decouple interactions between adjacent layers without introducing defects and impurity phases, and result in electron doping, which significantly alters the electronic and magnetic properties of NiPS$_3$. At an appropriate doping concentration (which is also achievable by electrostatic gating method), the AFM order in pristine NiPS$_3$ is switched to the FIM order with $T_c = 100$ K in THA-NiPS$_3$. At heavy doping concentration (TBA-NiPS$_3$, TPA-NiPS$_3$ and CTA-NiPS$_3$), the AFM order remains again. Such carrier doping tuned magnetic transition is due to the competition between Stoner exchange and super-exchange as the variation of the doping concentration. Our work provides a viable tool to modulate the magnetic properties of vdW magnets by electrical method, and opens a way for investigating strong correlation between electronic structure and magnetic properties of the vdW magnets and designing novel spintronic devices.

Methods

Sample preparation. $NiPS_3$ crystals were grown by vapor transport method. The mixture of stoichiometric high-purity Ni, P, S (Ni/P/S = 1:1:3) and iodine (10 mg/cm^3) as a transport agent were sealed into an evacuated quartz ampule and kept in a two-zone furnace (650 °C - 600 °C) for 1 week. The large single crystals will be harvested in the lower temperature end. Thin flakes of both pristine $NiPS_3$ and intercalated $NiPS_3$ were prepared on silicon substrate with a layer of 285 nm SiO_2 by mechanical exfoliation from bulk crystal using adhesive tape.

Electrochemical Intercalation. The electrochemical intercalation of $NiPS_3$ was carried out in a two-electrode system. The fresh $NiPS_3$ crystal was fixed on an electrode holder as the negative electrode (cathode), a piece of Pt was used as the positive electrode (anode), and tetraheptyl ammonium bromide (THA^+Br^-, Macklin, 98%) dissolved in acetonitrile (Macklin, 99%) at a concentration of 5 mg/ml was used as electrolyte. During the intercalation process, the voltage was slowly swept from 0 V to ~4 V at 50 °C. The electrochemical reaction consists of two half-reactions:

$$Br^- \longrightarrow \frac{1}{2}Br_2 + e^- \qquad (1),$$

$$NiPS_3 + x THA^+ + x e^- \longrightarrow (THA)_x NiPS_3 \qquad (2).$$
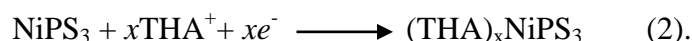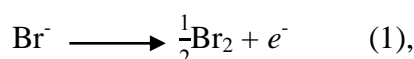
Two bromide ions lose electrons to form Br_2 at the anode, THA^+ cations are inserted into the vdW gaps of $NiPS_3$ (cathode), and $NiPS_3$ receives electrons from the external circuit. Therefore, organic cations intercalation causes electron doping of the sample. Intercalation of other organic cations, such as tetrabutyl ammonium (TBA^+), tetrapropyl ammonium (TPA^+), and cetyltrimethyl ammonium (CTA^+), share the same procedure as the THA^+.

Characterization. The X-ray diffraction (XRD) patterns were collected by SmartLab® high-resolution X-ray diffractometer (Rigaku, Japan) using Cu K_α radiation, λ = 1.5418 Å. The X-ray photoelectron spectroscopy (XPS) spectra were obtained in Nano-X by PHI-5000 Versaprobe II (Ulvac-Phi, Japan) using Al K_α X-ray ($h\nu$=1486.6 eV). The binding energies (BE) were calibrated with respect to the C-C 1 s bond (BE =284.8 eV). Raman spectra were collected by inVia™ confocal Raman microscope (Renishaw) using an excitation wavelength of 532 nm. The magnetic properties were measured by a vibrating sample magnetometer (VSM) of a commercial physical property measurement system (Dynacool-9, Quantum Design).

First-principles density functional theory (DFT) calculations. The Vanderbilt ultra-soft pseudopotential within exchange-correlation potential described by GGA+U, where U = 6 eV is applied on the Ni site[49]. We use the correction of DFT-D to consider the van der Waals interactions between layers[50]. For bulk computations, we construct a supercell of 20 atoms, and 8×5×7 k points mesh generated by Monkhorst-Pack scheme is used. The structure optimizations are performed until the force on each atom is less than 10^{-4} Ry/Bohr and the convergence threshold for

self-consistency is 10^{-8} Ry. The carrier doping is tuned by changing the total number of electrons adding in the cell, with a compensating jellium background of opposite charge to maintain charge neutrality.

Data availability.
All data supporting the findings of this work are available from the corresponding authors upon request.

References

1. Huang B*, et al.* Layer-dependent ferromagnetism in a van der Waals crystal down to the monolayer limit. *Nature* **546**, 270-273 (2017).

2. Gong C*, et al.* Discovery of intrinsic ferromagnetism in two-dimensional van der Waals crystals. *Nature* **546**, 265-269 (2017).

3. Burch KS, Mandrus D, Park J-G. Magnetism in two-dimensional van der Waals materials. *Nature* **563**, 47-52 (2018).

4. Gong C, Zhang X. Two-dimensional magnetic crystals and emergent heterostructure devices. *Science* **363**, aav4450 (2019).

5. Gibertini M, Koperski M, Morpurgo AF, Novoselov KS. Magnetic 2D materials and heterostructures. *Nat. Nanotechnol.* **14**, 408-419 (2019).

6. Mak KF, Shan J, Ralph DC. Probing and controlling magnetic states in 2D layered magnetic materials. *Nat. Rev. Phys.* **1**, 646-661 (2019).

7. Huang B*, et al.* Emergent phenomena and proximity effects in two-dimensional magnets and heterostructures. *Nat. Mater.* **19**, 1276-1289 (2020).

8. Jiang X*, et al.* Recent progress on 2D magnets: Fundamental mechanism, structural design and modification. *Appl. Phys. Rev.* **8**, 031305 (2021).

9. Li H, Ruan S, Zeng Y-J. Intrinsic van der Waals magnetic materials from bulk to the 2D limit: New frontiers of spintronics. *Adv. Mater.* **31**, 1900065 (2019).

10. Zhang Z*, et al.* Direct photoluminescence probing of ferromagnetism in monolayer two‐dimensional $CrBr_3$. *Nano Lett.* **19**, 3138-3142 (2019).

11. Deng YJ*, et al.* Gate-tunable room-temperature ferromagnetism in two-dimensional Fe_3GeTe_2. *Nature* **563**, 94-99 (2018).

12. Fei ZY*, et al.* Two-dimensional itinerant ferromagnetism in atomically thin Fe_3GeTe_2. *Nat. Mater.* **17**, 778-782 (2018).

13. May AF*, et al.* Ferromagnetism near room temperature in the cleavable van der Waals crystal Fe_5GeTe_2. *ACS Nano* **13**, 4436-4442 (2019).

14. Bonilla M*, et al.* Strong room-temperature ferromagnetism in VSe_2 monolayers on van der Waals substrates. *Nat. Nanotechnol.* **13**, 289-293 (2018).

15. Cai X*, et al.* Atomically thin $CrCl_3$: An in-plane layered antiferromagnetic insulator. *Nano Lett.* **19**, 3993-3998 (2019).

16. Kim K*, et al.* Suppression of magnetic ordering in XXZ-type antiferromagnetic monolayer $NiPS_3$. *Nat. Commun.* **10**, 345 (2019).

17. Lee J-U*, et al.* Ising-Type Magnetic Ordering in Atomically Thin $FePS_3$. *Nano Lett.* **16**, 7433-7438 (2016).

18. Kim K, *et al.* Antiferromagnetic ordering in van der Waals 2D magnetic material $MnPS_3$ probed by Raman spectroscopy. *2D Mater.* **6**, 041001 (2019).

19. Coak MJ, *et al.* Tuning dimensionality in van-der-Waals antiferromagnetic Mott insulators $TMPS_3$. *J. Phys. Condens. Matter* **32**, 124003 (2019).

20. Peng Y, *et al.* Magnetic structure and metamagnetic transitions in the van der Waals antiferromagnet $CrPS_4$. *Adv. Mater.* **32**, 2001200 (2020).

21. Otrokov MM, *et al.* Prediction and observation of an antiferromagnetic topological insulator. *Nature* **576**, 416-422 (2019).

22. Jiang S, Shan J, Mak KF. Electric-field switching of two-dimensional van der Waals magnets. *Nat. Mater.* **17**, 406-410 (2018).

23. Wang Y, *et al.* Strain-sensitive magnetization reversal of a van der Waals magnet. *Adv. Mater.* **32**, 2004533 (2020).

24. Jiang S, Li LZ, Wang ZF, Mak KF, Shan J. Controlling magnetism in 2D CrI_3 by electrostatic doping. *Nat. Nanotechnol.* **13**, 549-553 (2018).

25. Huang B, *et al.* Electrical control of 2D magnetism in bilayer CrI_3. *Nat. Nanotechnol.* **13**, 544-548 (2018).

26. Verzhbitskiy IA, *et al.* Controlling the magnetic anisotropy in $Cr_2Ge_2Te_6$ by electrostatic gating. *Nat. Electron.* **3**, 460-465 (2020).

27. Wang Z, *et al.* Electric-field control of magnetism in a few-layered van der Waals ferromagnetic semiconductor. *Nat. Nanotechnol.* **13**, 554-559 (2018).

28. Wang NZ, *et al.* Transition from ferromagnetic semiconductor to ferromagnetic metal with enhanced Curie temperature in $Cr_2Ge_2Te_6$ via organic ion intercalation. *J. Am. Chem. Soc.* **141**, 17166-17173 (2019).

29. Joy PA, Vasudevan S. Magnetism in the layered transition-metal thiophosphates MPS_3 (M=Mn, Fe, and Ni). *Phys. Rev. B* **46**, 5425-5433 (1992).

30. Wildes AR, *et al.* Magnetic structure of the quasi-two-dimensional antiferromagnet $NiPS_3$. *Phys. Rev. B* **92**, 224408 (2015).

31. Kim SY, *et al.* Charge-spin correlation in van der Waals antiferromagnet $NiPS_3$. *Phys. Rev. Lett.* **120**, 136402 (2018).

32. Yan M, *et al.* Correlations in the electronic structure of van der Waals $NiPS_3$ crystals: An X-ray absorption and resonant photoelectron spectroscopy study. *J. Phys. Chem. Lett.* **12**, 2400-2405 (2021).

33. Chittari BL, *et al.* Electronic and magnetic properties of single-layer MPX_3 metal phosphorous trichalcogenides. *Phys. Rev. B* **94**, 184428 (2016).

34. Li X, Wu X, Yang J. Half-metallicity in $MnPSe_3$ exfoliated nanosheet with carrier doping. *J. Am. Chem. Soc.* **136**, 11065-11069 (2014).

35. Zhou J, *et al.* Layered intercalation materials. *Adv. Mater.* **33**, 2004557 (2021).

36. Wang C, *et al.* Monolayer atomic crystal molecular superlattices. *Nature* **555**, 231-236 (2018).

37. He Q, *et al.* In situ probing molecular intercalation in two-dimensional layered semiconductors. *Nano Lett.* **19**, 6819-6826 (2019).

38. Shi MZ, *et al.* Organic-ion-intercalated FeSe-based superconductors. *Phys. Rev. Mater.* **2**, 074801 (2018).

39. Zhang H, *et al.* Enhancement of superconductivity in organic-inorganic hybrid topological materials. *Sci. Bull.* **65**, 188-193 (2020).

454 40. Bao W, *et al.* Approaching the limits of transparency and conductivity in graphitic materials
455   through lithium intercalation. *Nat. Commun.* **5**, 4224 (2014).

456 41. Susner MA, Chyasnavichyus M, McGuire MA, Ganesh P, Maksymovych P. Metal thio- and
457   selenophosphates as multifunctional van der Waals layered materials. *Adv. Mater.* **29**, 1602852
458   (2017).

459 42. Kuo C-T, *et al.* Exfoliation and raman spectroscopic fingerprint of few-layer $NiPS_3$ van der
460   Waals crystals. *Sci. Rep.* **6**, 20904 (2016).

461 43. Foot PJS, *et al.* The structures and conduction mechanisms of lithium-intercalated and
462   lithium-substituted nickel phosphorus trisulphide ($NiPS_3$), and the use of the material as a
463   secondary battery electrode. *Phys. Stat. Sol. (a)* **100**, 11-29 (1987).

464 44. Basnet R, Wegner A, Pandey K, Storment S, Hu J. Highly sensitive spin-flop transition in
465   antiferromagnetic van der Waals material MPS_3 (M=Ni and Mn). *Phys. Rev. Mater.* **5**, 064413
466   (2021).

467 45. Cong X, Liu X-L, Lin M-L, Tan P-H. Application of Raman spectroscopy to probe
468   fundamental properties of two-dimensional materials. *npj 2D Mater. Appl.* **4**, 13 (2020).

469 46. Currò GM, Grasso V, Neri F, Silipigni L. The effects of the lithium intercalation on the X-ray
470   photoelectron spectra of $NiPS_3$. *Il Nuovo Cimento D* **17**, 37-52 (1995).

471 47. Giannozzi P, *et al.* QUANTUM ESPRESSO: a modular and open-source software project for
472   quantum simulations of materials. *J. Phys. Condens. Matter* **21**, 395502 (2009).

473 48. Giunta G, Grasso V, Neri F, Silipigni L. Electrical conductivity of lithium-intercalated
474   thiophosphate $NiPS_3$ single crystals. *Phys. Rev. B* **50**, 8189-8194 (1994).

475 49. Cococcioni M, de Gironcoli S. Linear response approach to the calculation of the effective
476   interaction parameters in the LDA+U method. *Phys. Rev. B* **71**, 035105 (2005).

477 50. Grimme S. Semiempirical GGA-type density functional constructed with a long-range
478   dispersion correction. *J. Comput. Chem.* **27**, 1787-1799 (2006).

Author contributions

Y.L.W. conceived the project. B.S. grew bulk $NiPS_3$ crystals. M.J.M. performed the electrochemical intercalation, Raman, and AFM measurements under the supervision of Y.L.W.. S.L.W. and M.J.M. performed the VSM measurements under the supervision of S.P.W., B.L.H. and Y.L.W.. X.W.Z. performed the first-principles calculations under the supervision of X.H.L. M.J.M., Y.Z., H.N.S performed XRD measurements under the supervision of Y.X.C.. M.J.M. performed XPS measurements under the supervision of F.S.L.. M.J.M., L.X.Y., H.X. performed electrical conductivity measurements. M.J.M., X.W.Z., X.H.L., and Y.L.W. wrote the manuscript, and all authors participated in discussing the results and revising the manuscript.

498   **Competing interests:** The authors declare no competing interests.